



# Enhanced photocatalytic degradation of methyl orange by coconut shell-derived biochar composites under visible LED light irradiation

Yean Ling Pang<sup>1,2</sup> · Zhi Xuan Law<sup>1</sup> · Steven Lim<sup>1,2</sup> · Yin Yin Chan<sup>1</sup> · Siew Hoong Shuit<sup>1,2</sup> · Woon Chan Chong<sup>1,2</sup> · Chin Wei Lai<sup>3</sup>

Received: 18 June 2020 / Accepted: 26 December 2020 / Published online: 28 January 2021  
© The Author(s), under exclusive licence to Springer-Verlag GmbH, DE part of Springer Nature 2021

## Abstract

The conversion of carbon-rich biomass into valuable material is an environmental-friendly approach for its reutilization. In this study, coconut shell-derived biochar, graphitic carbon nitride (g-C<sub>3</sub>N<sub>4</sub>), g-C<sub>3</sub>N<sub>4</sub>/biochar, titanium dioxide (TiO<sub>2</sub>)/biochar, zinc oxide (ZnO)/biochar, and ferric oxide (Fe<sub>2</sub>O<sub>3</sub>)/biochar were synthesized and characterized by using scanning electron microscopy coupled with energy-dispersive X-ray spectroscopy (SEM-EDX), X-ray diffraction (XRD), Fourier-transform infrared spectroscopy (FTIR), thermogravimetric analysis (TGA), surface area analysis, UV-Vis diffuse reflectance spectroscopy (DRS), and zeta potential analysis. The g-C<sub>3</sub>N<sub>4</sub> or metal oxide particles were found to be well-distributed on the coconut shell-derived biochar with the improvement in thermal stability and enlargement of specific surface area. A great reduction in band gap energy was observed in the composite materials after incorporating with the biochar. Among different biochar composites, g-C<sub>3</sub>N<sub>4</sub>/biochar was found to have the highest photocatalytic activity. The interactive effect of parameters such as catalyst dosage, peroxymonosulfate (PMS) oxidant dosage, and solution pH on the photocatalytic degradation of methyl orange was investigated using the response surface methodology (RSM). The highest photocatalytic degradation efficiency (96.63%) was achieved at catalyst dosage of 0.75 g/L, oxidant dosage of 0.6 mM, and solution pH 3 after 30 min.

**Keywords** Photocatalytic · Coconut shell-derived biochar · Graphitic carbon nitride (g-C<sub>3</sub>N<sub>4</sub>) · Characterizations · Optimization

## Introduction

Methyl orange is a typical anionic azo dye that is often reported as the most stable and is particularly difficult to be degraded using conventional methods such as adsorption, biological treatment, and coagulation, owing to the stability of aromatic groups (Ahmad et al. 2020). The efficient degradation of methyl orange is necessary from an environmental perspective

due to the toxicity and carcinogenic and mutagenic properties to human health (Zou and Wang 2019). In order to overcome this issue, advanced oxidation processes (AOPs) have appeared as alternative technologies to conventional dye removal methods. Conventional biological methods are usually insufficient to decompose complex dye molecules such as methyl orange with many aromatic rings due to the highly resistant to microorganisms (Husain et al. 2019). Meanwhile, the adsorption and coagulation process merely transfer organic pollutants from one phase to another phase to reduce the concentration rather than mineralizing them. Photocatalysis is able to generate highly reactive free radicals such as hydroxyl radicals ( $\cdot\text{OH}$ ) which have the ability to oxidize and mineralize most of the organic pollutants into smaller inorganic products such as carbon dioxide and water completely without secondary pollution (El Nemr et al. 2018). The generation and separation of charge carriers for holes ( $h^+$ ) and electrons ( $e^-$ ) upon light irradiation, leading to the formation of reactive oxygen species on the surface of oxides, such as  $h^+$ , hydroxyl radicals ( $\cdot\text{OH}$ ), superoxide anions ( $\cdot\text{O}_2^-$ ), and singlet oxygen ( $^1\text{O}_2$ ) (Mauček et al. 2018).

Responsible editor: Sami Rtimi

✉ Yean Ling Pang  
pangyl@utar.edu.my

<sup>1</sup> Department of Chemical Engineering, Lee Kong Chian Faculty of Engineering and Science, Universiti Tunku Abdul Rahman, 43000 Kajang, Selangor, Malaysia

<sup>2</sup> Centre for Photonics and Advanced Materials Research, Universiti Tunku Abdul Rahman, 43000 Kajang, Selangor, Malaysia

<sup>3</sup> Nanotechnology & Catalysis Research Centre (NANOCAT), Institute of Graduate Studies Building, University of Malaya, 50603 Kuala Lumpur, Malaysia

The most common studied photocatalysts are titanium dioxide (TiO<sub>2</sub>), zinc oxide (ZnO), and iron oxide (Fe<sub>2</sub>O<sub>3</sub>) due to their interesting characteristics such as low cost, low toxicity, high stability, and high catalytic activity. The wide band gap energies for TiO<sub>2</sub> and ZnO are about 3.2 and 3.37 eV, respectively, which restrict the light absorption to UV region which accounts for only 5% of the solar spectrum. On the other hand, graphitized-carbon nitride (g-C<sub>3</sub>N<sub>4</sub>) as a metal-free organic polymeric visible-light-driven semiconductor has attracted huge attention to be investigated as a photocatalyst, owing to its non-toxicity, inexpensiveness, high stability, visible light absorption ability, and no heavy metal pollution. Though the bandgap energies of g-C<sub>3</sub>N<sub>4</sub> and Fe<sub>2</sub>O<sub>3</sub> are about 2.7 eV (Ahmad 2020) and 2.1 eV (Yuan et al. 2020), respectively, the rapid recombination of photo-generated electron-hole carriers and low surface area restrict the photocatalytic pollutant degradation towards environmental remediation. Therefore, modification of these potential materials is the best way to overcome the faced obstacle.

Most of the current research on the photocatalytic degradation of methyl orange was primarily focused on the investigation of metal- or non-metal-based semiconductors instead of biomass feedstock materials. In recent years, the application of raw biomass as an adsorbent in the wastewater treatment process arises worldwide, but it possesses limitations such as poor porosity, low specific surface area, and poor cation exchange capacity. This poor adsorption capability could be improved by converting biomass into activated carbon or biochar (Tsamo et al. 2019). Biochar is a low-cost and carbon-rich material produced from pyrolysis of biomass under the condition of limiting oxygen. Biochar contains an abundance of functional groups such as –OH, –COOH, C=O, and –NH<sub>2</sub>, which provide a strong adsorption capacity for various types of pollutants and can be easily tuned with other functional materials (Lu et al. 2019). Thus, biochar has become a research hotspot as new and excellent support for photocatalysts due to its well-developed mesoporous structure, semiconductor characteristics, good adsorption, and stability (Chen et al. 2019; Shan et al. 2020). Immobilizations of photocatalyst onto suitable support, especially for the carbon material, an electron acceptor, can prevent the recombination of h<sup>+</sup> and e<sup>-</sup>, improved the utilization of solar energy due to the implantation of carbon element, and experienced synergistic reaction of adsorption and photocatalysis (Peng et al. 2019; Shan et al. 2020). By connecting both high catalytic of photocatalyst and a low cost, waste reuse, and good adsorption capacity of biochar, it is believed that this new material may provide an economical and effective method for photocatalytic degradation of methyl orange.

Coconut shell contains a large number of biodegradable and non-toxic substances such as glucan and xylan (Liu et al. 2020) and composition of 33.30% lignin, 30.58% cellulose, 26.70% hemicellulose, 8.86% water, and 0.56% ash

(Nunes et al. 2020). Besides, coconut shell also comprises a variety of chemical or functional groups such as acetamido, amino, amide, sulfhydryl, sulfate, carboxyl, and hydroxyl (Li et al. 2018), which endows the coconut shell superior hydrophilic property and suitable to be processed for activated carbon or biochar (Liu et al. 2020).

Hence, in this work, composite materials were synthesized through the incorporation of several types of metal and metal-free semiconductors with coconut shell-derived biochar in order to enhance their physical, chemical, and optical properties. The relationship between these semiconductors and biochar towards the photocatalysis was examined by incorporating main characterization methods. To the best of our knowledge, no studies are available which have assessed the potential usage of coconut shell biochar material incorporated with several types of semiconductors under LED light irradiation. This constitutes the key innovation in this research study. The photocatalytic activities were performed through the degradation of methyl orange under LED lamp irradiation. In addition, kinetic study and response surface methodology (RSM) were also carried out to have a better understanding on the photocatalytic degradation process and determine the optimum condition of the reaction, respectively.

## Experiment

### Chemicals and materials

Methyl orange, methylene blue, and congo red were purchased from R&M Chemicals, while rhodamine B and reactive blue were obtained from Sigma-Aldrich. Malachite green was purchased from Fisher Scientific. Metal oxide and g-C<sub>3</sub>N<sub>4</sub> precursors including zinc nitrate (Zn(NO<sub>3</sub>)<sub>2</sub>, 99%), potassium carbonate (K<sub>2</sub>CO<sub>3</sub>, 99.5%), titanium isopropoxide (TTIP, 97%), ferric chloride (FeCl<sub>3</sub>, 99%), ammonium hydroxide (NH<sub>4</sub>OH, 25%), and melamine (C<sub>3</sub>H<sub>6</sub>N<sub>6</sub>, 99%), as well as oxidants, which included hydrogen peroxide (H<sub>2</sub>O<sub>2</sub>, 37%), potassium persulfate (PS, 99%), and potassium hydrogen monopersulfate (PMS, 45%) were obtained from Merck. All the chemicals were used as received.

### Preparation of biochar and biochar composites

Coconut shells were collected and cut into smaller pieces. After rinsing with distilled water, coconut shells were dried in oven at 80 °C for 12 h. The dried coconut shells were calcined under N<sub>2</sub> environment at 500 °C for 2 h to produce the biochar. TiO<sub>2</sub>/biochar was synthesized using sol-gel method. Biochar was dispersed in 40 mL of water under ultrasonication for 15 min, followed by the addition of 10 mL of TTIP and 40 mL of ethanol. After that, the solution was stirred at ambient temperature for 1 h and left for 24 h to

obtain gel. The gel was dried in oven at 80 °C for 12 h and the powder was calcined at 500 °C for 2 h to yield the TiO<sub>2</sub>/biochar.

ZnO/biochar and Fe<sub>2</sub>O<sub>3</sub>/biochar were synthesized using the co-precipitation method. To synthesize ZnO/biochar, biochar was first dispersed in 100 mL of water. Next, 0.03 M of Zn(NO<sub>3</sub>)<sub>2</sub> and 0.05 M of K<sub>2</sub>CO<sub>3</sub> were added into the solution under continuous stirring. The solution was stirred at ambient temperature for 1 h for the precipitation of zinc carbonate. For Fe<sub>2</sub>O<sub>3</sub>/biochar composite, biochar was dispersed in 150 mL of water prior to the addition of 6 g FeCl<sub>3</sub>. After that, 2 mL of NH<sub>4</sub>OH was added dropwise into the solution. The solution was stirred at ambient temperature for 1 h for the precipitation of ferric hydroxide. For both cases, the solid products were rinsed, dried, and calcined in the same condition as the preparation of TiO<sub>2</sub>/biochar to produce respective metal oxide composites.

For the preparation of g-C<sub>3</sub>N<sub>4</sub>/biochar, melamine was used as the precursor of g-C<sub>3</sub>N<sub>4</sub>. Biochar and melamine were dispersed in 100 mL of distilled water under ultrasonication for 15 min. After stirring at ambient temperature for 1 h, the mixture was rinsed, dried, and calcined at the same condition for the preparation of TiO<sub>2</sub>/biochar to produce g-C<sub>3</sub>N<sub>4</sub>/biochar. For all the composite materials, the weight percentage of metal oxides and g-C<sub>3</sub>N<sub>4</sub> to biochar were set at 1.

## Sample characterization

SEM was conducted to analyze the surface morphological of the synthesized samples by using the Hitachi Model S-3400N scanning electron microscope. The elemental composition was determined by energy-dispersive X-ray spectroscopy. XRD analysis was carried out to identify the crystalline structure of samples using Shimadzu XRD-600. To determine the functional groups of the samples, attenuated total reflectance (ATR) sampling technique was used using Nicolet IS 10 Fourier-transform infrared spectroscopy. FTIR spectra of the samples were recorded in the wavenumber range of 4000 to 400 cm<sup>-1</sup>. The thermal stability of the synthesized samples was analyzed through TGA by means of a Perkin Elmer thermal analyzer STA 8000. All the samples were subjected to heating, with temperature ranging from 30 to 1000 °C under a heating rate of 10 °C/min.

For surface area analysis, 0.5 g of each sample was first degassed at 150 °C to remove impurities. The Brunauer-Emmett-Teller (BET) surface area, pore size, and pore volume of the samples were measured based on nitrogen adsorption-desorption data at 77.35 K employing a surface analyzer of Micrometrics ASAP-2020. For particle surface charge analysis, the zeta potential of the samples was measured at 25 °C by using Horiba SZ-100-Z. Typically, 5 mg of sample powder was dispersed in 50 mL of 0.001 M NaCl solution through ultrasonication for 15 min. To obtain the isoelectric point, the

pH of the suspension was adjusted to pH 2, 4, 6, 8, and 10 through the addition of HCl and NaOH. Three zeta potential readings were taken at every solution pH and the average zeta potential value was plotted against the solution pH.

UV-Vis DRS was conducted to determine the absorbance and band gap energy of the sample. The absorbances of the synthesized samples were examined with the wavelength range from 300 to 800 nm. The indirect band gap energies of the samples were determined from the Kubelka-Munk function:  $F(R) = (1 - R)^2/2R$ , where  $R$  is the diffuse reflectance and the Wood-Tauc plot is  $[F(R) \times h\nu]^{1/2}$  where  $\nu$  is the photon frequency, and  $h$  is Planck's constant, by extrapolation of the straight line to the abscissa (Costa et al. 2020).

## Photocatalytic degradation of methyl orange

In a typical study, 100 mL of 10 mg/L methyl orange solution was prepared in a beaker. After that, 1 g/L of the synthesized sample was added as a catalyst, followed by 30 min of stirring under the dark condition to achieve equilibrium adsorption-desorption state. Then, the solution was irradiated by visible light irradiation (Philips LED lamp 20W). The sample solution was collected in a 5-min interval and subjected to liquid sample analysis. During analysis, the absorbance of methyl orange was measured using a UV-Vis spectrophotometer (PG Instruments T60) at its maximum absorbance wavelength of 464 nm. The degradation efficiency was calculated via Eq. (1).

$$\text{Degradation efficiency (\%)} = [(C_0 - C_t)/C_0] \times 100\% \quad (1)$$

where,  $C_0$  is the initial concentration of dye (mg/L) and  $C_t$  is the concentration of dye at time interval (mg/L).

## Results and discussion

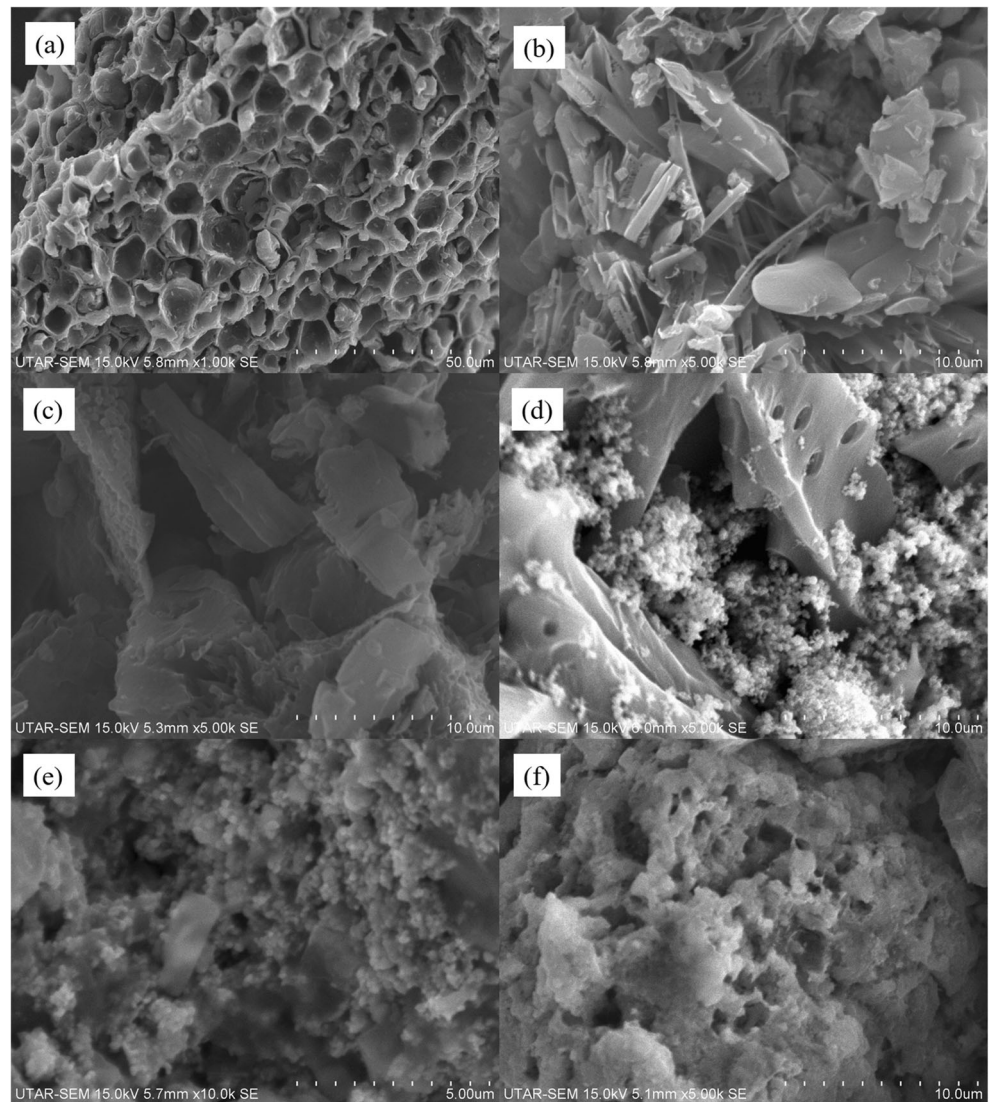
### Characterizations

#### SEM-EDX study

Figure 1 illustrates the SEM images of the synthesized biochar, g-C<sub>3</sub>N<sub>4</sub>, g-C<sub>3</sub>N<sub>4</sub>/biochar, and other metal oxides/biochar. The pore diameters of biochar were about 5–8 μm as shown in Fig. 1a. The developed macropores were due to the release of volatile compounds during the pyrolysis of coconut shell biomass (Zhang et al. 2020). These highly porous structures could act as adsorption sites and proved the ability of biochar as an effective adsorbent. Figure 1b shows the surface morphology of g-C<sub>3</sub>N<sub>4</sub> present in the form of small flakes with observable strip textures, which was a typical structural feature of g-C<sub>3</sub>N<sub>4</sub> synthesized through thermal decomposition



**Fig. 1** SEM images of **a** biochar, **b** g-C<sub>3</sub>N<sub>4</sub>, **c** g-C<sub>3</sub>N<sub>4</sub>-biochar, **d** TiO<sub>2</sub>-biochar, **e** ZnO-biochar, and **f** Fe<sub>2</sub>O<sub>3</sub>-biochar



as reported by Li et al. (2019a). The average length of g-C<sub>3</sub>N<sub>4</sub> was found to be around 5 μm. For the surface morphology of g-C<sub>3</sub>N<sub>4</sub>/biochar as shown in Fig. 1c, the structure of g-C<sub>3</sub>N<sub>4</sub> remained unchanged though being incorporated in the biochar skeleton. This composite material showed a porous and flake-like structure, proving that both substances retained their pristine structures.

The surface morphology of TiO<sub>2</sub>/biochar illustrated that TiO<sub>2</sub> granules were well dispersed on the biochar with little agglomeration as shown in Fig. 1d, e shows the ZnO particles exhibited a spherical shape and the majority were found to be in the form of aggregates once distributed on the biochar. Figure 1f shows that Fe<sub>2</sub>O<sub>3</sub> particles were present in the cluster form and exhibited an extremely high degree of agglomeration once distributed on biochar.

The EDX results of particles are shown in Table 1. Generally, biochar was mainly composed of carbon and oxygen. The C/N atomic ratio of pure g-C<sub>3</sub>N<sub>4</sub> was 0.69, which

was close to the ideal value of 0.75. The concentration of nitrogen which exceeded the stoichiometric ratio in this study was mainly due to the incomplete combustion of melamine (Li et al. 2019a). Besides, the carbon element present in the g-C<sub>3</sub>N<sub>4</sub>/biochar was found to be higher than the pristine g-C<sub>3</sub>N<sub>4</sub> due to the incorporation of biochar. In addition, both ZnO/biochar and Fe<sub>2</sub>O<sub>3</sub>/biochar showed impurity elements such as potassium and chlorine. This was primarily due to the usage of K<sub>2</sub>CO<sub>3</sub> and FeCl<sub>3</sub> during the synthesis of ZnO and Fe<sub>2</sub>O<sub>3</sub>, respectively. Furthermore, a low carbon weight percentage found in both composite materials might be due to the fact that aggregated metal oxide particles were fully distributed and covered on the biochar.

#### XRD study

The XRD results of biochar, g-C<sub>3</sub>N<sub>4</sub>, g-C<sub>3</sub>N<sub>4</sub>/biochar, and other metal oxides/biochar are shown in Fig. 2. The broad

**Table 1** EDX results of the prepared samples

Catalyst	C (%)		O (%)		N (%)		Ti (%)		Zn (%)		Fe (%)		K (%)		Cl (%)	
	Wt	At	Wt	At	Wt	At	Wt	At	Wt	At	Wt	At	Wt	At	Wt	At
Biochar	88.77	91.32	11.23	8.68	–	–	–	–	–	–	–	–	–	–	–	–
g-C <sub>3</sub> N <sub>4</sub>	37.15	40.80	–	–	62.85	59.20	–	–	–	–	–	–	–	–	–	–
g-C <sub>3</sub> N <sub>4</sub> -BC	51.54	55.36	–	–	48.46	44.64	–	–	–	–	–	–	–	–	–	–
TiO <sub>2</sub> -BC	39.65	56.01	32.02	33.96	–	–	28.33	10.03	–	–	–	–	–	–	–	–
ZnO-BC	12.17	27.23	24.86	41.76	–	–	–	–	44.44	18.27	–	–	18.53	12.74	–	–
Fe <sub>2</sub> O <sub>3</sub> -BC	17.09	36.89	22.54	30.32	–	–	–	–	–	–	32.45	15.06	–	–	27.92	17.73

peak observed about 25° in the coconut shell–derived biochar was assigned to the (002) plane in carbon material with an amorphous structure (Chen et al. 2019). For pure g-C<sub>3</sub>N<sub>4</sub>, the characteristic peaks observed at 13° and 27° were attributed to the diffraction of (100) and (002) planes of g-C<sub>3</sub>N<sub>4</sub>, respectively. According to Li et al. (2019a), the peak observed at 13° was originated from the repeating tri-s-triazine ring structure, while the peak presented at 27° resulted from the accumulation of interlayers along the *c*-axis of the conjugated aromatic structure, which exhibited a graphite structure. It was noticed that both peak intensities at 13° and 27° in g-C<sub>3</sub>N<sub>4</sub>/biochar were reduced, indicating that the incorporation of biochar inhibited the formation of bulk layered g-C<sub>3</sub>N<sub>4</sub> during the melamine polycondensation process (Yu et al. 2013).

The XRD pattern of TiO<sub>2</sub>/biochar showed diffraction peaks at 25°, 38°, 48°, 54°, and 56°, which were corresponding to the reflection from (101), (004), (200), (105), and (211) planes of TiO<sub>2</sub>, respectively. All these peaks were attributed to anatase-TiO<sub>2</sub> and no additional peak was found for rutile and brookite phases. For ZnO/biochar, the diffraction peaks at 32°, 34°, 36°, 47°, and 57° were assigned to the reflection from (100), (002), (101), (102), and (110) crystal planes of ZnO,

respectively (Gholami et al. 2019). For Fe<sub>2</sub>O<sub>3</sub>/biochar, the diffraction peaks that appeared at 33°, 36°, 44°, and 54° were attributed to the (104), (110), (113), and (116) planes of a rhombohedral structure of α-Fe<sub>2</sub>O<sub>3</sub>, which proved that α-Fe<sub>2</sub>O<sub>3</sub> was the only metal oxide presented in the composite material (Chen et al. 2019). For all the metal oxide composites, the characteristic peak of biochar at 25° could not be seen clearly in the XRD patterns which were possibly owing to the coverage of aggregated metal oxide particles on the surface of the carbon structure.

**FTIR study**

The results obtained from the FTIR analyses of biochar, g-C<sub>3</sub>N<sub>4</sub>, g-C<sub>3</sub>N<sub>4</sub>/biochar, and other metal oxides/biochar are shown in Fig. 3. For pure biochar, a broad absorption peak appeared at 3376 cm<sup>-1</sup> was owing to the –OH bond stretching vibration (Chen et al. 2019). The absorption peaks at 1557 cm<sup>-1</sup> and 1148 cm<sup>-1</sup> were attributed to the presence of C=C bond in the aromatic ring and C–O bond, respectively (Zhang et al. 2018b). Besides, a weak absorption band at 744 cm<sup>-1</sup> indicated that the C–H bond was present in the

**Fig. 2** XRD patterns of **a** biochar, **b** g-C<sub>3</sub>N<sub>4</sub>, **c** g-C<sub>3</sub>N<sub>4</sub>-biochar, **d** TiO<sub>2</sub>-biochar, **e** ZnO-biochar, and **f** Fe<sub>2</sub>O<sub>3</sub>-biochar

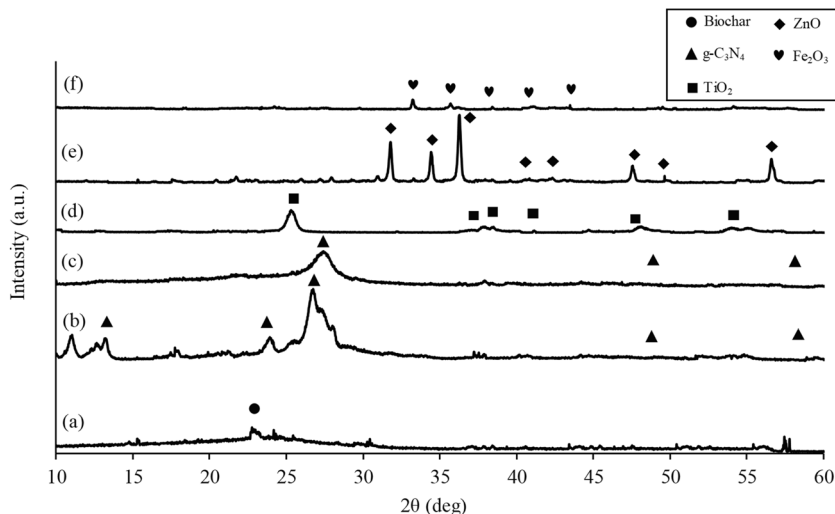
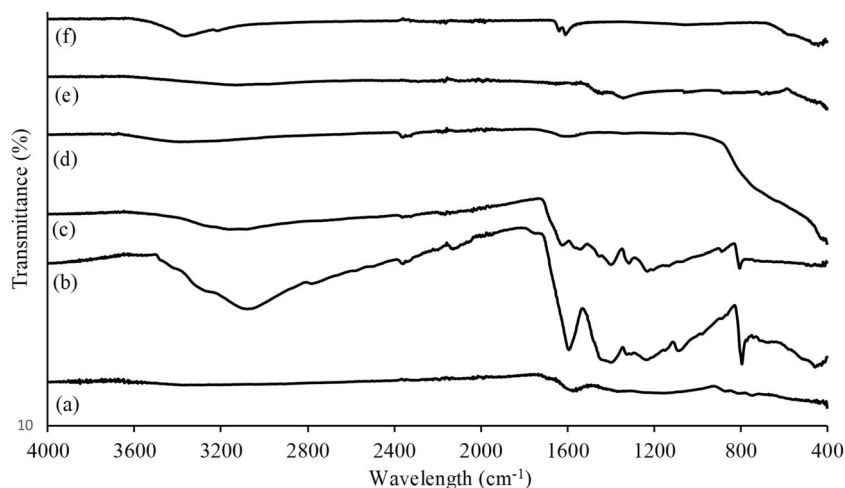


**Fig. 3** FTIR spectra of **a** biochar, **b** g-C<sub>3</sub>N<sub>4</sub>, **c** g-C<sub>3</sub>N<sub>4</sub>-biochar, **d** TiO<sub>2</sub>-biochar, **e** ZnO-biochar, and **f** Fe<sub>2</sub>O<sub>3</sub>-biochar



coconut shell-derived biochar. For pure g-C<sub>3</sub>N<sub>4</sub>, the broad peak centered at 3080 cm<sup>-1</sup> was corresponding to the stretching vibration of primary (-NH<sub>2</sub>) and secondary (=NH) amine group (Zhu et al. 2015). Besides, the strong band at 794 cm<sup>-1</sup> was derived from the intense bending vibration mode of the tri-s-triazine unit (Zhu et al. 2015). In addition, g-C<sub>3</sub>N<sub>4</sub> presented a series of absorption bands at 1593 cm<sup>-1</sup>, 1397 cm<sup>-1</sup>, 1232 cm<sup>-1</sup>, and 1088 cm<sup>-1</sup>, which were attributed to the stretching vibration of C-N heterocycles (Li et al. 2019a, b). The FTIR spectrum of g-C<sub>3</sub>N<sub>4</sub>/biochar was substantially similar to the pure g-C<sub>3</sub>N<sub>4</sub>, which indicated that the incorporation of biochar did not alter the bulk structure of g-C<sub>3</sub>N<sub>4</sub>.

FTIR spectrum of TiO<sub>2</sub>/biochar showed a broad absorption peak from 400 to 700 cm<sup>-1</sup>, which was assigned to the stretching vibration of the Ti-O bond, indicating the existence of TiO<sub>2</sub> in the composite material (Lu et al. 2019). Besides, the FTIR spectrum showed the Zn-O peak from 400 to 600 cm<sup>-1</sup>, suggesting the formation of ZnO on the composite material. The stretching mode of the Fe-O bond was found at the peak of 500 cm<sup>-1</sup>, confirming the incorporation of Fe<sub>2</sub>O<sub>3</sub> in the composite material (Chen et al. 2019). For all the metal oxide/biochar, the absorption band at around 3300 cm<sup>-1</sup> and 1600 cm<sup>-1</sup> was related to the stretching and bending vibration of the -OH group, respectively (Lu et al. 2019).

### TGA analysis

Figure 4 shows the TGA curves of biochar, g-C<sub>3</sub>N<sub>4</sub>, g-C<sub>3</sub>N<sub>4</sub>/biochar, and metal oxide/biochar ranging from 30 to 1000 °C at a heating rate of 10 °C/min. The heating process could be divided into the water evaporation stage and decomposition stage. At the first stage, a minor weight loss of less than 10% within the temperature of 30 °C to 100 °C was noted in the TGA curves of biochar, g-C<sub>3</sub>N<sub>4</sub>, g-C<sub>3</sub>N<sub>4</sub>/biochar, and TiO<sub>2</sub>/biochar due to the evaporation of moisture contents. Meanwhile, ZnO/biochar and Fe<sub>2</sub>O<sub>3</sub>/biochar showed a

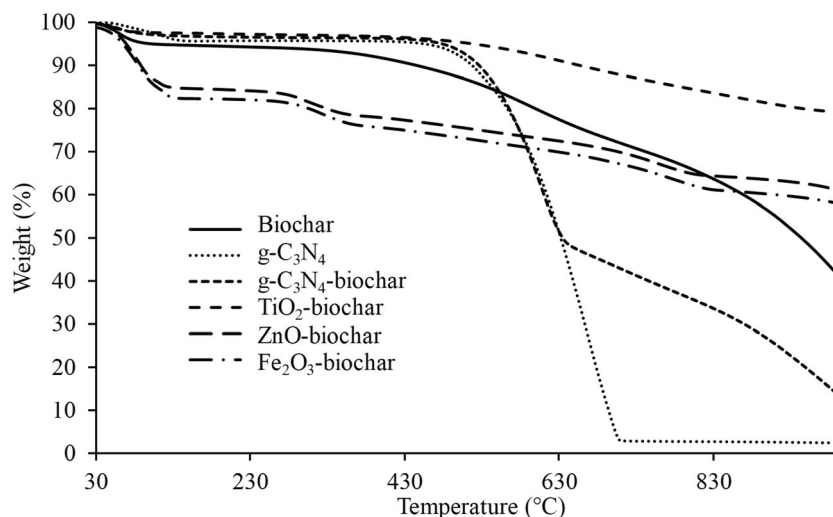
significant weight loss of around 20% was mainly related to the physisorbed and chemisorbed water molecules during the co-precipitation synthesis process (Mian et al. 2019).

The decomposition process of biochar started at 350 °C and the residual ash content was around 42% at 1000 °C. Both the g-C<sub>3</sub>N<sub>4</sub> and g-C<sub>3</sub>N<sub>4</sub>/biochar started to decompose at 500 °C, with a similar decomposing rate within a heating temperature of 500 to 650 °C. g-C<sub>3</sub>N<sub>4</sub> was completely decomposed at 700 °C (Han et al. 2020), while g-C<sub>3</sub>N<sub>4</sub>/biochar had a residual ash content of 15% when the heating temperature reached 1000 °C. These results suggested that biochar could improve the thermal stability of g-C<sub>3</sub>N<sub>4</sub>. Besides, the total weight loss of TiO<sub>2</sub>/biochar was about 20%, which was the lowest among the composite materials. This might be related to the high purity and high thermal stability of TiO<sub>2</sub>/biochar with less amount of water and organic compounds attached to the sample. Meanwhile, ZnO/biochar and Fe<sub>2</sub>O<sub>3</sub>/biochar started to decompose at a relatively low temperature of 300 °C and their total weight losses at 1000 °C were 39% and 42%, respectively.

### Surface area analysis

Table 2 shows the BET surface area, pore volume, and pore size of biochar, g-C<sub>3</sub>N<sub>4</sub>, g-C<sub>3</sub>N<sub>4</sub>/biochar, and metal oxide/biochar. The surface area and pore volume of all the composite materials were higher than the biochar sample. Generally, large surface area and high pore volume could facilitate the adsorption of dye molecules and provide numerous surface reaction sites for the photocatalytic activity to take place (Fazal et al. 2020). Meanwhile, mesoporous structures could facilitate rapid diffusion of reactant molecules passed through the pores (Maučec et al. 2018). However, the high surface area is commonly associated with a large number of defects, acted as charge trapping sites where recombination takes place during the photocatalytic sequence, and led to a lower catalytic activity (Nandi and Das 2019). Besides, the photocatalytic

**Fig. 4** TGA curves of biochar, g-C<sub>3</sub>N<sub>4</sub>, g-C<sub>3</sub>N<sub>4</sub>-biochar, TiO<sub>2</sub>-biochar, ZnO-biochar, and Fe<sub>2</sub>O<sub>3</sub>-biochar under nitrogen atmosphere



ability of a sample is strongly dependent not only on the surface area and pore volume; other material properties like composition, band gap energy, phase structure, crystal size, crystallinity, particles size, surface hydroxyl group, and surface defect also played important roles for efficient degradation performance.

According to the IUPAC classification (Kruk and Jaroniec 2001), all the composite samples exhibited a mesoporous structure with the pore size ranging from 2 to 50 nm. The surface area of coconut shell-derived biochar was 1.224 m<sup>2</sup>/g, which was slightly lower than the pure g-C<sub>3</sub>N<sub>4</sub> (2.075 m<sup>2</sup>/g). When biochar and g-C<sub>3</sub>N<sub>4</sub> were incorporated, the surface area of the composite material increased moderately to 5.242 m<sup>2</sup>/g. It was suggested that the presence of a biochar skeleton could prevent excessive accumulation of g-C<sub>3</sub>N<sub>4</sub> and achieved a higher surface area (Li et al. 2019b). Besides, the surface area of TiO<sub>2</sub>/biochar and ZnO/biochar was 158.575 m<sup>2</sup>/g and 183.104 m<sup>2</sup>/g, respectively. These results were probably caused by the small grain size of the metal oxides during the synthesis process.

Figure 5a shows the nitrogen adsorption-desorption isotherms of catalyst samples. All of the samples exhibited a typical type IV isotherm according to the IUPAC classification (Kruk and Jaroniec 2001), which indicated the adsorption of nitrogen proceeds via multilayer adsorption followed by capillary condensation. The isotherms of biochar, g-C<sub>3</sub>N<sub>4</sub>, g-

C<sub>3</sub>N<sub>4</sub>/biochar, and Fe<sub>2</sub>O<sub>3</sub>/biochar showed the type of H1 hysteresis loop, which belongs to a typical characteristic of porous material with cylindrical pore geometry (Peng et al. 2020). Meanwhile, TiO<sub>2</sub>/biochar and ZnO/biochar showed an H3 hysteresis loop, which indicated a slit-shaped pore structure with a degree of disorder (Silvestri et al. 2019b).

The pore size distribution of samples calculated from the Barrett–Joyner–Halenda (BJH) method is presented in Fig. 5b. It could be observed that TiO<sub>2</sub>/biochar and ZnO/biochar had a narrow pore size distribution with an average pore size at about 10–11 nm, indicating the existence of mesopores in the composite materials. Meanwhile, biochar, g-C<sub>3</sub>N<sub>4</sub>, g-C<sub>3</sub>N<sub>4</sub>/biochar, and Fe<sub>2</sub>O<sub>3</sub>/biochar showed an increment in the pore size distributions, which indicated that the samples might consist of some coexisting mesopores and macropores structures. In short, the composite materials had a pore structure of different sizes and volumes could facilitate charge transfer and enhance the photocatalytic activity of the materials (Silvestri et al. 2019a).

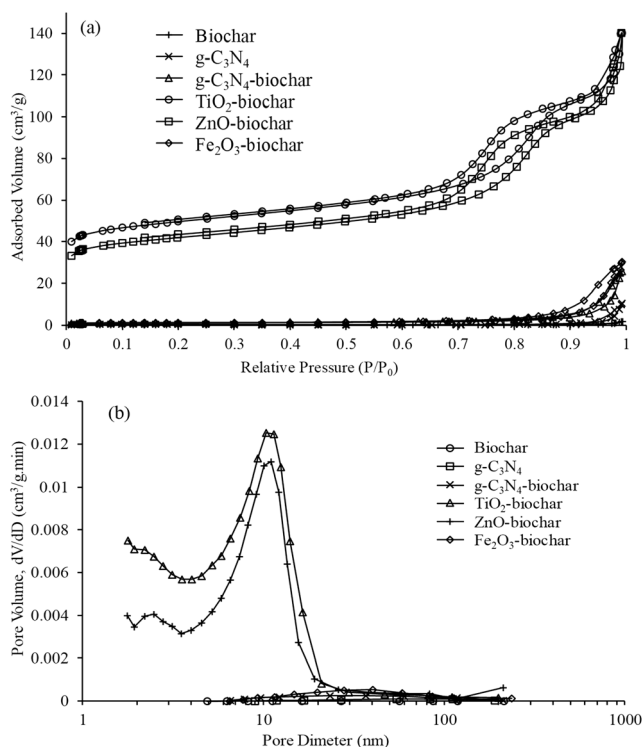
**UV-Vis DRS**

Figure 6a shows the UV-Vis DRS absorption spectra of g-C<sub>3</sub>N<sub>4</sub>, g-C<sub>3</sub>N<sub>4</sub>/biochar, TiO<sub>2</sub>/biochar, ZnO/biochar, and Fe<sub>2</sub>O<sub>3</sub>/biochar. It was observed that the spectra for g-C<sub>3</sub>N<sub>4</sub>/biochar experienced a shift to longer wavelength (red shift)

**Table 2** BET surface area, pore size and pore volume of the samples

Samples	Surface area (m <sup>2</sup> /g)	Pore volume (cm <sup>3</sup> /g)	Pore size (nm)
Biochar	1.224	0.003	50.041
g-C <sub>3</sub> N <sub>4</sub>	2.074	0.004	54.913
g-C <sub>3</sub> N <sub>4</sub> /biochar	5.242	0.017	36.847
TiO <sub>2</sub> /biochar	158.575	0.168	11.480
ZnO/biochar	183.104	0.178	10.435
Fe <sub>2</sub> O <sub>3</sub> /biochar	5.222	0.030	28.868





**Fig. 5** **a** Nitrogen adsorption-desorption isotherms and **b** pore size distribution of biochar, g-C<sub>3</sub>N<sub>4</sub>, g-C<sub>3</sub>N<sub>4</sub>-biochar, TiO<sub>2</sub>-biochar, ZnO-biochar, and Fe<sub>2</sub>O<sub>3</sub>-biochar

and showed a higher visible light absorption as compared with g-C<sub>3</sub>N<sub>4</sub>. This indicated that the incorporation of low reflectivity biochar could improve the optical absorption property of the composite material significantly and increased wavelength of the absorption edge from about 450 to 500 nm (Li et al. 2019b). It was reported that both pure TiO<sub>2</sub> and ZnO showed absorbance in the UV region (200–400 nm) only with absorption edges located at about 380 nm and 390 nm, respectively (Wang et al. 2018). Meanwhile, pure biochar exhibited a distinct absorption in the visible range owing to the black color of the material (Fazal et al. 2020). Meng et al. (2020) reported that the thick black layer of biochar would block the absorption of visible light, resulting in decreased photocatalytic efficiency. However, an appropriate amount of biochar in composite materials could retain the semiconductor polymeric framework and enhanced photocatalytic performance. When both TiO<sub>2</sub> and ZnO composited with biochar, these samples exhibited noticeable absorbance in the visible range (400–700 nm), which indicated the absorption in the visible range was attributed to the biochar content. The high absorbance in the UV region also confirmed the presence of metal oxide, whereas the absorption intensity within the visible range was ascribed to be induced by the biochar content. Similar results had been reported in the literature to demonstrate the usefulness of the biochar-based composites (Xie et al. 2019; Fazal et al. 2020). The wavelength of the absorption edge for Fe<sub>2</sub>O<sub>3</sub> was usually shorter than 600 nm due to the intrinsic band gap

absorption of Fe<sub>2</sub>O<sub>3</sub> (Zhang et al. 2018a). However, it was clearly showed that the steep absorption edge of Fe<sub>2</sub>O<sub>3</sub>/biochar was extended to above 600 nm, which indicated the interaction between Fe<sub>2</sub>O<sub>3</sub> and biochar where Fe<sub>2</sub>O<sub>3</sub> responded well to visible light. Besides, all these composite materials which are more responsive to solar light may also be ascribed to the C incorporation to form C–O–metal/non-metal bonds and mid-gap energy state formation (Norouzi et al. 2019).

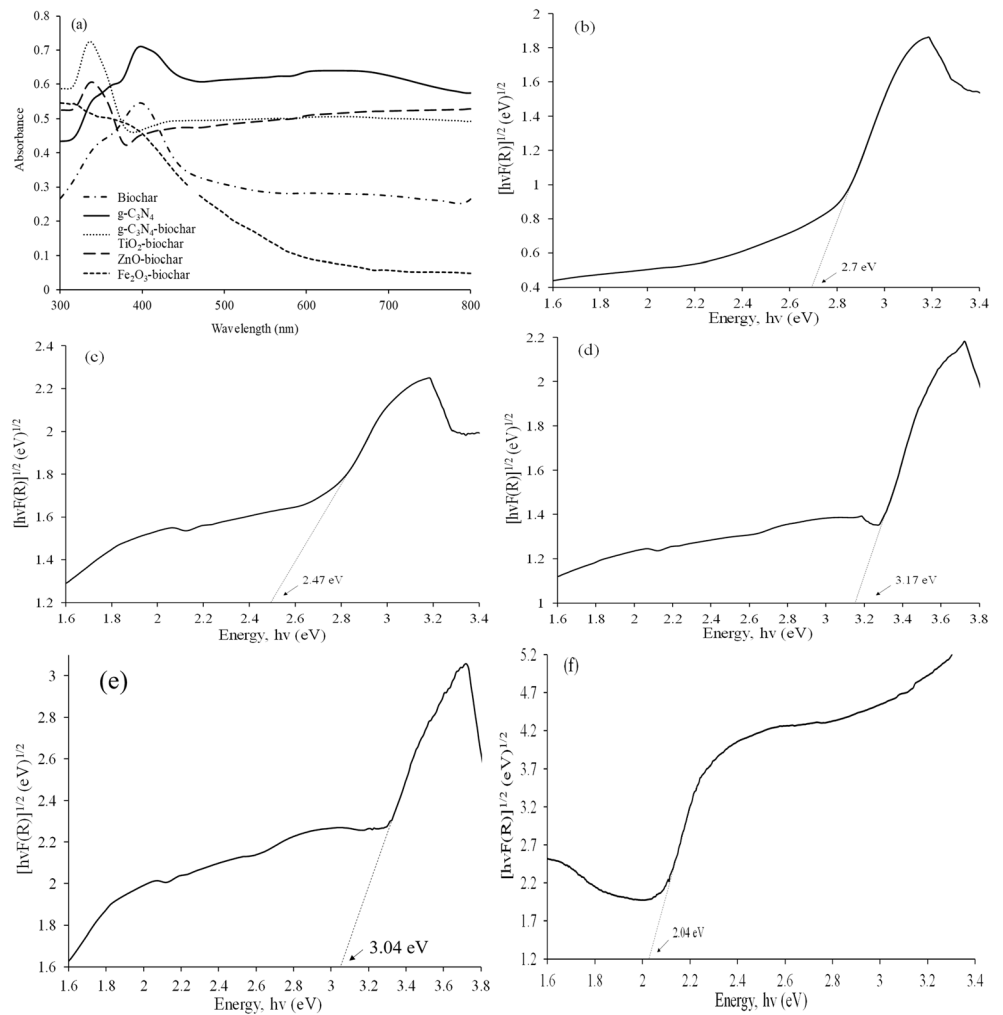
The band gap energies of the samples were further calculated from the UV–vis DRS spectra based on the transformed Kubelka-Munk function as depicted in Fig. 6b–f. By applying Tauc's relation, a graph of  $(h\nu F(R))^{1/2}$  versus photon energy was plotted and a tangent line was drawn to obtain the band gap energy of the sample. The band gap energies of g-C<sub>3</sub>N<sub>4</sub>, g-C<sub>3</sub>N<sub>4</sub>/biochar, TiO<sub>2</sub>/biochar, ZnO/biochar, and Fe<sub>2</sub>O<sub>3</sub>/biochar were found to be 2.7 eV, 2.47 eV, 3.17 eV, 3.04 eV, and 2.04 eV, respectively. The band gap energies of all the synthesized metal oxides/biochar were slightly lower than the pure metal oxides, in which the typical band gap energies of TiO<sub>2</sub>, ZnO, and Fe<sub>2</sub>O<sub>3</sub> are 3.2 eV, 3.3 eV, and 2.2 eV, respectively (Lu et al. 2019; Das et al. 2019). According to Li et al. (2019a), the incorporation of a biochar skeleton could facilitate a photocatalyst to capture more visible light and adjust its optical properties through the electronic excitation process. Furthermore, it was reported that the incorporation of semiconductors with a carbon matrix could create vacancies, which led to band gap narrowing (Gholami et al. 2019). Though a smaller band gap energy material is usually more desired for efficient absorption by solar light, the band gap must also be large enough to meet the thermodynamics and kinetics requirements for effective overall water splitting reaction to proceed (Zhou et al. 2012; Nasir et al. 2019). Thus, g-C<sub>3</sub>N<sub>4</sub>/biochar composite material was expected to exhibit better photocatalytic performance as it could harvest more visible light than the pure g-C<sub>3</sub>N<sub>4</sub> and the band gap energy potential levels of Fe<sub>2</sub>O<sub>3</sub> were not within the redox potential for proton reduction and water oxidation potential levels.

### Zeta potential analysis

Zeta potential analysis was conducted to investigate the surface charge of biochar, g-C<sub>3</sub>N<sub>4</sub>, and g-C<sub>3</sub>N<sub>4</sub>/biochar at different solution pH. Generally, particles exhibit protonation and deprotonation in aqueous suspension, which could be attributed to the interaction with H<sup>+</sup> or OH<sup>-</sup> ions from the aqueous medium at the surface of the particle. Under different solution pH, the extent of these interactions could be diverse, thereby resulting in different surface charges and zeta potential values (Zhu et al. 2015). The isoelectric point is the pH value in which a zero net charge is attained. As displayed in Fig. 7, the isoelectric points of biochar, g-C<sub>3</sub>N<sub>4</sub>, and g-C<sub>3</sub>N<sub>4</sub>/biochar were pH 2.2, 4.0, and 3.7, respectively. The particles' surface is positively charged at pH below the isoelectric point and it is



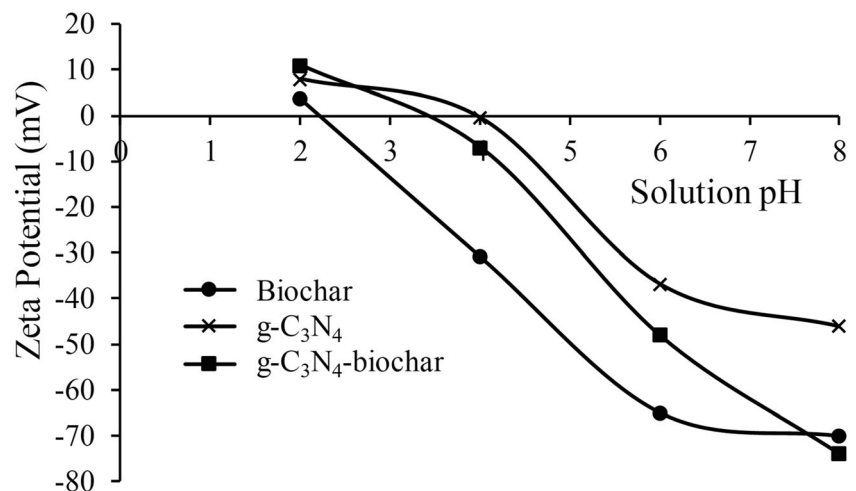
**Fig. 6** **a** UV-Vis absorption spectra and band gap energies of **b** g-C<sub>3</sub>N<sub>4</sub>, **c** g-C<sub>3</sub>N<sub>4</sub>-biochar, **d** TiO<sub>2</sub>-biochar, **e** ZnO-biochar, and **f** Fe<sub>2</sub>O<sub>3</sub>-biochar



negatively charged at pH above the isoelectric point. For instance, g-C<sub>3</sub>N<sub>4</sub>/biochar composites possess a negatively charged surface, which favored the adsorption of cationic dyes via electrostatic attraction at pH above 3.7 (Pi et al. 2015). It is reported that the dissociation constants (pK<sub>a</sub>) of methyl

orange which is about 3.7 (Karimi-Shamsabadi et al. 2017), when pH is lower than pK<sub>a</sub> of methyl orange, methyl orange is in zwitterion form, which promoted dye adsorption on the catalyst surface and its photocatalytic degradation. When pH is higher than pK<sub>a</sub> of methyl orange, methyl orange is in the

**Fig. 7** Zeta potential analysis results of biochar, g-C<sub>3</sub>N<sub>4</sub>, and g-C<sub>3</sub>N<sub>4</sub>-biochar



azo form. Some researchers found that the photocatalytic oxidation efficiency was increased as increasing the solution pH due to the number of hydroxyl ions as the main precursor of hydroxyl radicals increases (Mirzaei et al. 2018). However, at pH values more than the pKa of methyl orange, the g-C<sub>3</sub>N<sub>4</sub>/biochar surface and methyl orange are both negatively charged. Therefore, the degradation efficiency is anticipated to be decreased as increasing the pH value due to the repulsion force.

## Photocatalytic degradation of methyl orange

### Effect of different catalyst

The effect of various types of catalysts on the photocatalytic degradation of methyl orange was studied and the results are shown in Fig. 8. It was found that g-C<sub>3</sub>N<sub>4</sub>/biochar demonstrated the highest degradation efficiency of methyl orange among all the pure and composite materials. This was mainly due to the narrow band gap energy of g-C<sub>3</sub>N<sub>4</sub>/biochar (2.47 eV) and meets the redox potential for proton reduction and water oxidation potential levels. The excitation of an electron from the valence band to the conduction band in the visible light region could also be induced to generate more free radicals, which were highly reactive in the mineralization of organic dye. Meanwhile, the photocatalytic activity of Fe<sub>2</sub>O<sub>3</sub>/biochar was significantly lower than the g-C<sub>3</sub>N<sub>4</sub>/biochar, even though it had narrower band gap energy (2.11 eV). It was reported that the photocatalytic activity of Fe<sub>2</sub>O<sub>3</sub> was limited owing to a very short hole-diffusion length (2–4 nm) (Qin et al. 2017) and the conduction band edge was below the reduction potential of the proton reduction (H<sup>+</sup>/H<sub>2</sub>) redox pair which was ineffective for water splitting process (Zhou et al. 2012). On the other hand, TiO<sub>2</sub>/biochar and ZnO/biochar had the lower photocatalytic efficiencies of Methyl Orange among the composite materials though both materials possess high surface

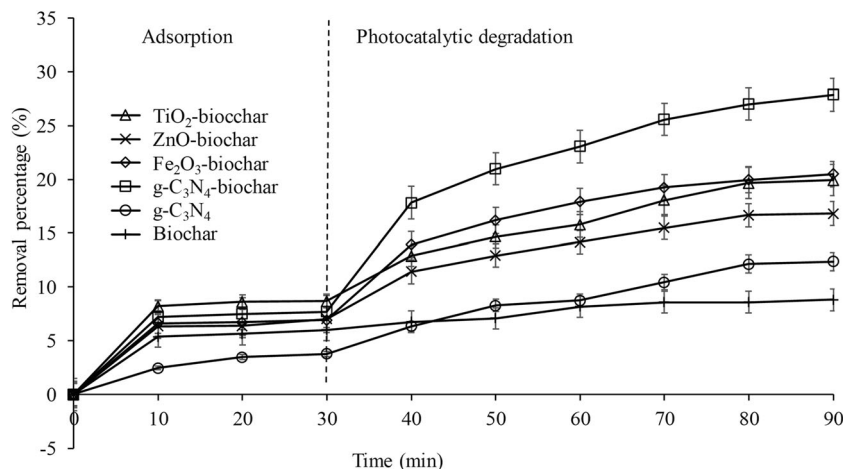
area. This indicated that other material properties such as composition, band gap energy, phase structure, crystal size, crystallinity, particle size, surface hydroxyl group, and surface defect did play a significant role in determining high catalytic activity. For instance, the large band gap energies of TiO<sub>2</sub>/biochar (3.17 eV) and ZnO/biochar (3.02 eV) might restrict the absorption of the visible light spectrum for the excitation process, thus reducing the production of free reactive radicals in the photocatalytic degradation of organic dye.

The findings showed that biochar was a good adsorbent, but it barely had catalytic performance in dye degradation. Meanwhile, pure g-C<sub>3</sub>N<sub>4</sub> exhibited lower photocatalytic activity as compared to g-C<sub>3</sub>N<sub>4</sub>/biochar, which might be due to its wider band gap energy (2.7 eV), lower surface area, and weaker visible light absorption. According to Li et al. (2019b), the intimate interface between g-C<sub>3</sub>N<sub>4</sub> and amorphous carbon in biochar could accelerate the charge transfer kinetics and prolong the lifetime of charge carriers. This was because the carbon-rich materials could serve as an electron collector and transporter in a composite material, which could delay the recombination rate of electron-hole pairs. Besides, the composite materials with the larger surface area could provide more active sites for the photocatalytic activity to take place.

### Kinetic study

Kinetic studies were performed based on the photocatalytic degradation rate of methyl orange to identify the reaction order kinetic model. Figure 9a shows the pseudo-first-order kinetic for the photocatalytic degradation of methyl orange under different operating temperatures. The high determination of coefficient ( $R^2 > 0.95$ ) revealed that all the data were fitted well to the pseudo-first-order kinetic model as presented in Eq. (2). Gholami et al. (2019) reported that the reaction order of dye degradation could be determined by the concentration of dye at different time intervals. This was mainly due to the

**Fig. 8** Effect of different catalyst on the photocatalytic degradation of methyl orange (adsorption = 0 to 30 min; photocatalysis = 30 to 90 min)



short half-life of oxidative radicals ( $\cdot\text{OH}$  and  $\text{SO}_4^{\cdot-}$ ), where their concentrations were not likely to be identified and measured, thus considered the constant value at a specific time.

$$\ln(C_0/C_t) = k_{\text{app}}t \tag{2}$$

where  $C_0$  is the initial concentration of dye (mg/L),  $C_t$  is the concentration of dye at time interval (mg/L),  $k_{\text{app}}$  is the apparent reaction rate constant ( $\text{min}^{-1}$ ), and  $t$  is the reaction time (min).

The  $k_{\text{app}}$  values were found increasing with the increasing temperature implying that the reaction was accelerated by the increment in the reaction temperature. Generally, the temperature dependence of  $k_{\text{app}}$  is related to the Arrhenius Law which is shown in Eq. (3).

$$k_{\text{app}} = A \exp(-E_a/RT) \tag{3}$$

where  $E_a$  is the activation energy in unit Joules/mole,  $R$  is the gas constant with the value of 8.314 J/mol K, and  $T$  is the reaction temperature expressed in unit K. Figure 9b shows a linear relationship between the variables through the derivation of Arrhenius equation by having  $\ln k_{\text{app}}$  and  $1/T$  as the responding and manipulating variables, respectively, and the equations are presented in Eqs. (4) and (5).

$$\ln k_{\text{app}} = -E_a/RT + \ln A \tag{4}$$

$$\ln k_{\text{app}} = -2600.8 (1/T) + 5.862 \tag{5}$$

Hence, the activation energy needed to initiate the reaction could be evaluated from the gradient of the linear graph. The calculated  $E_a$  value of photocatalytic degradation of methyl orange in the presence of g- $\text{C}_3\text{N}_4$ /biochar was found to be 21.62 kJ/mol. This value was higher than the activation energy for the diffusion-controlled reactions (10–13 kJ/mol), which indicated that photocatalytic degradation of methyl orange was dominated by the rate of intrinsic chemical reactions on the catalyst surface rather than the rate of mass transfer (Yao et al. 2014). Besides, the calculated  $E_a$  value lied within the range of 15.8–75.5 kJ/mol for the reactions using different heterogeneous catalysts (Guo et al. 2018).

### Optimization study

In the optimization study, three experimental parameters, i.e., catalyst dosage ( $X_1$ ), oxidant dosage ( $X_2$ ), and solution pH ( $X_3$ ), were considered and selected as the independent variables while the photocatalytic degradation efficiency of methyl orange ( $Y$ ) was chosen as the response of the study. The ranges and levels of the independent variables were set according to the previous parameter studies. The central

composite design (CCD) model was used to examine the interactive relationship between the participating variables. As shown in Table 3, the resulting photocatalytic degradation efficiency of methyl orange falls in the range from 43.82 to 94.39% in response to the variation in the experimental conditions. A quadratic model with significant terms was obtained for the prediction of photocatalytic degradation efficiency of methyl orange and their empirical relations could be explained using Eq. (6). The positive and negative value of the coefficients indicated the synergistic and antagonistic effect of the methyl orange degradation, respectively (Mohammad et al. 2019).

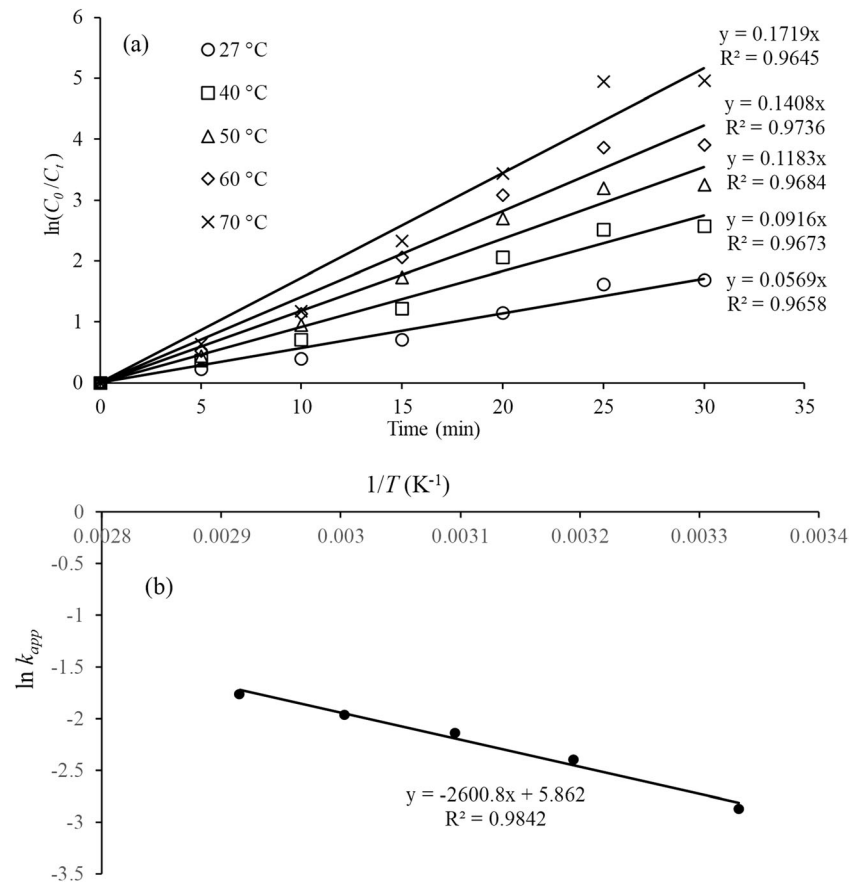
$$Y = 87.29 + 2.70 X_1 + 14.32 X_2 - 7.11 X_3 - 0.1950 X_1 X_2 - 0.8475 X_1 X_3 - 0.6275 X_2 X_3 - 4.51 X_1^2 - 6.80 X_2^2 - 7.94 X_3^2 \tag{6}$$

The accuracy of the model was justified by an analysis of variance (ANOVA) and the results are presented in Table 4. The model  $F$ -value of 994.03 implied that the model developed was significant and there was only 0.01% of the chance that the  $F$ -value could occur due to noise. On the other hand,  $P$  value indicated the probability of getting results bigger than the  $F$ -value and was used to test the null hypothesis. Generally, parameters having  $P$  value less than 0.05 were said to be significant (Armah et al. 2020). In this case, the model terms  $X_1$ ,  $X_2$ ,  $X_3$ ,  $X_1 X_2$ ,  $X_1 X_3$ ,  $X_2 X_3$ ,  $X_1^2$ ,  $X_2^2$ , and  $X_3^2$  were significant. Therefore, this analysis confirmed the significance of all the individual variables and interaction terms in the photocatalytic degradation of methyl orange. Furthermore, the lack-of-fit  $F$ -value of 2.55 indicated that the lack of fit was not significant relative to the pure error. The non-significant lack of fit indicated good predictability of the model and there was only a 16.42% chance that the lack-of-fit  $F$ -value could occur due to noise.

A high value of determination coefficient ( $R^2 = 0.9989$ ) implied that 99.89% of the total variation for the photocatalytic degradation of methyl orange could be described by the suggested model. Besides, the value of adequate precision which measured the signal-to-noise ratio was found to be 91.9289, indicating that the model had an adequate signal. Generally, an adequate precision ratio greater than 4 implied that the developed model could be used to navigate the design space (Armah et al. 2020).

Figure 10 shows the response surface plots of photocatalytic degradation to study the interactive effect of the independent variables. The degradation efficiency increased by changing the PMS oxidant dosage from 0.2 to 0.6 mM in a certain catalyst dosage at the fixed value of solution pH 5. This result confirmed the experimental result obtained from the previous one parameter at a time study, where the optimum oxidant dosage was found to be 0.6 mM. This was primarily

**Fig. 9** **a** Pseudo-first-order kinetic plot for photocatalytic degradation of methyl orange, **b** Arrhenius plot of  $\ln k_{app}$  versus  $1/T$



due to the increasing amount of  $\cdot\text{OH}$  and  $\text{SO}_4^{\cdot-}$  as increasing the PMS oxidant dosage. Figure 10a also shows the increment

of catalyst dosage from 0.25 to 0.75 g/L resulted in the increment in dye degradation efficiency, which was mainly

**Table 3** Experimental results for the three independent variables

Standard order	Point type	Coded independent variable levels			Degradation efficiency (%)	
		Catalyst dosage, g/L ( $X_1$ )	PMS oxidant dosage, mM ( $X_2$ )	Solution pH ( $X_3$ )	Experimental values	Predicted values
1	Factorial	0.25 (-1)	0.2 (-1)	3.0 (-1)	57.34	56.47
2	Factorial	0.75 (+1)	0.2 (-1)	3.0 (-1)	64.01	63.95
3	Factorial	0.25 (-1)	0.6 (+1)	3.0 (-1)	86.72	86.75
4	Factorial	0.75 (+1)	0.6 (+1)	3.0 (-1)	94.39	93.45
5	Factorial	0.25 (-1)	0.2 (-1)	7.0 (+1)	44.49	45.20
6	Factorial	0.75 (+1)	0.2 (-1)	7.0 (+1)	49.55	49.29
7	Factorial	0.25 (-1)	0.6 (+1)	7.0 (+1)	73.14	72.97
8	Factorial	0.75 (+1)	0.6 (+1)	7.0 (+1)	75.64	76.28
9	Axial	0.08 (-1.68)	0.4 (0)	5.0 (0)	69.93	69.99
10	Axial	0.92 (+1.68)	0.4 (0)	5.0 (0)	78.81	79.06
11	Axial	0.5 (0)	0.06 (-1.68)	5.0 (0)	43.82	43.99
12	Axial	0.5 (0)	0.74 (+1.68)	5.0 (0)	92.00	92.15
13	Axial	0.5 (0)	0.4 (0)	1.64 (-1.68)	75.83	76.81
14	Axial	0.5 (0)	0.4 (0)	8.36 (+1.68)	53.55	52.89
15	Center	0.5 (0)	0.4 (0)	5.0 (0)	86.81	87.29
16	Center	0.5 (0)	0.4 (0)	5.0 (0)	88.14	87.29
17	Center	0.5 (0)	0.4 (0)	5.0 (0)	86.93	87.29
18	Center	0.5 (0)	0.4 (0)	5.0 (0)	87.23	87.29
19	Center	0.5 (0)	0.4 (0)	5.0 (0)	86.83	87.29
20	Center	0.5 (0)	0.4 (0)	5.0 (0)	87.87	87.29



**Table 4** ANOVA results for photocatalytic degradation efficiency of methyl orange

Factors	Squares sum	Freedom degrees	Square average	F-value	Probability, P value	
Quadratic model	5180.05	9	575.56	994.03	<0.0001	Significant
$X_1$	99.35	1	99.35	171.58	<0.0001	
$X_2$	2799.44	1	2799.44	4834.82	<0.0001	
$X_3$	690.53	1	690.53	1192.59	<0.0001	
$X_1 X_2$	3.04	1	3.04	5.25	0.0485	
$X_1 X_3$	5.75	1	5.75	9.92	0.0103	
$X_2 X_3$	3.15	1	3.15	5.44	0.0419	
$X_1^2$	293.49	1	293.49	506.88	<0.0001	
$X_2^2$	665.74	1	665.74	1149.78	<0.0001	
$X_3^2$	907.44	1	907.44	1567.21	<0.0001	
Residual	5.79	10	0.5790			
Lack of fit	4.16	5	0.8314	2.55	0.1642	Insignificant
Pure error	1.63	5	0.3267			
Corrected total	5185.84	19				

$R^2 = 0.9989$ ; adequate precision = 91.9289

attributed to the availability of more catalytic active sites. It was noted that PMS oxidant dosage was a more significant

variable in determining the degradation efficiency of methyl orange as compared to the catalyst dosage. For example, by

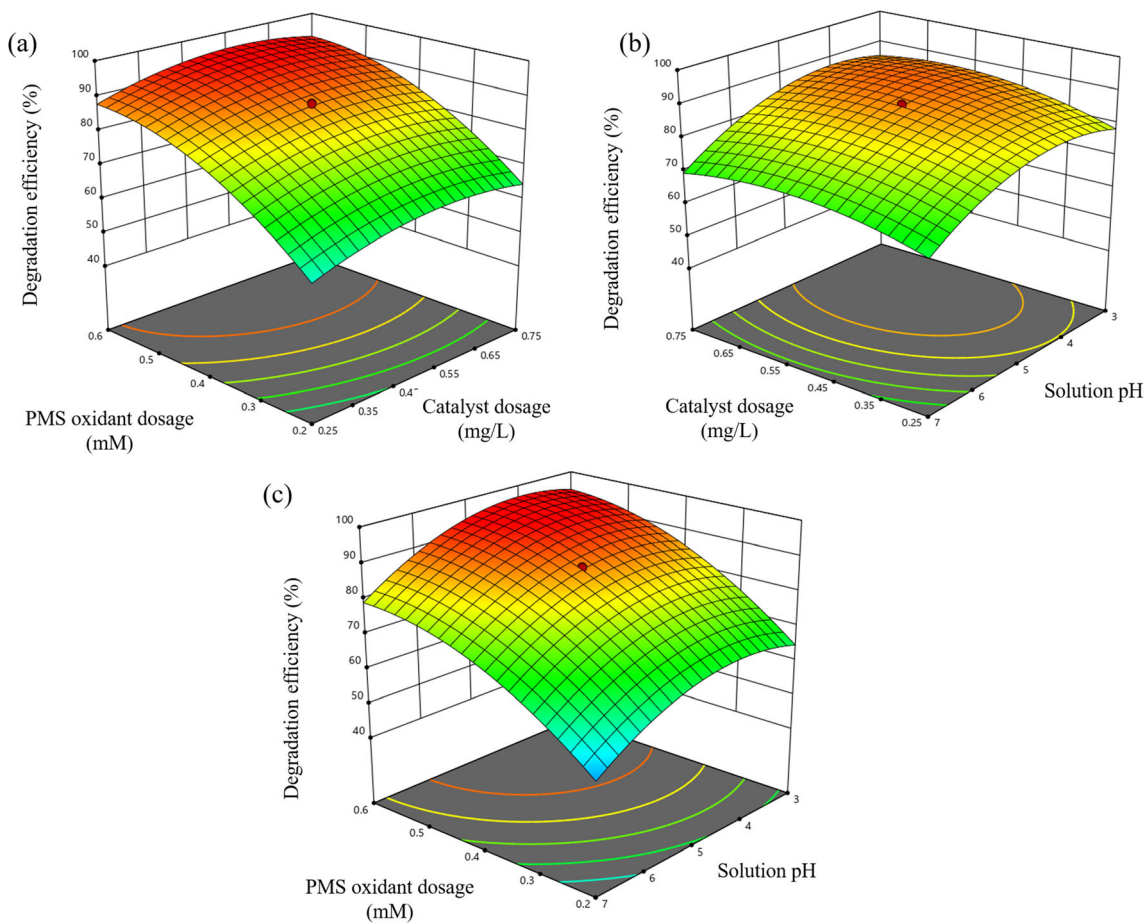


**Fig. 10** Three-dimensional surface plots of the photocatalytic degradation of methyl orange at fixed **a** solution pH 3, **b** oxidant dosage 0.4 mM, and **c** catalyst dosage 0.5 g/L

**Table 5** Experimental and predicted results conducted at optimized condition for model validation

Runs	Catalyst dosage, g/L ( $X_1$ )	PMS oxidant dosage, mM ( $X_2$ )	Solution pH ( $X_3$ )	Degradation efficiency (%)	
				Experimental values	Predicted values
1	0.75	0.57	3.48	96.63	94.86
2	0.63	0.52	3.57	94.27	95.16
3	0.66	0.52	3.88	92.78	95.05
4	0.55	0.54	3.59	93.91	95.89
5	0.53	0.57	4.52	95.71	96.18

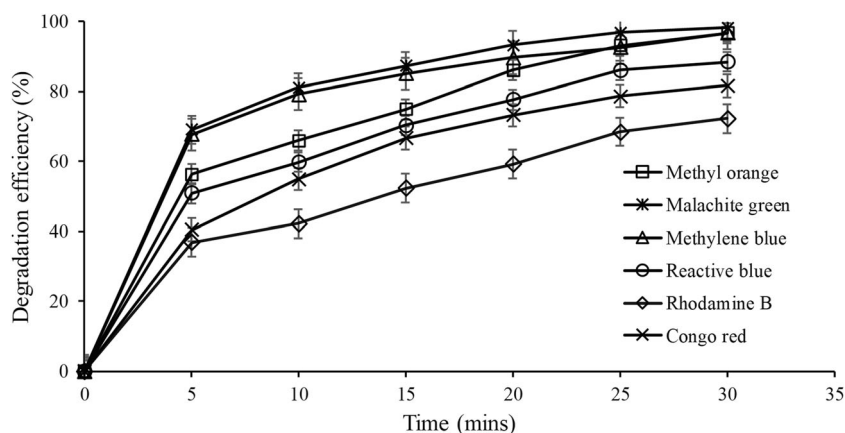
comparing run 1 with run 3 and run 1 with run 2, the interaction between these two factors could be observed. The degradation efficiency increased from 57.34 to 86.72% when the PMS oxidant dosage increased from 0.2 to 0.6 mM under constant catalyst dosage and solution pH. Meanwhile, the degradation efficiency enhanced slightly from 57.34 to 64.01% as the catalyst dosage increased from 0.25 to 0.75 g/L under constant oxidant dosage and solution pH. The results showed that PMS oxidant dosage had a greater effect on the photocatalytic degradation of Methyl Orange as compared to the catalyst dosage.

The interaction between catalyst dosage and solution pH at an oxidant dosage of 0.4 mM is shown in Fig. 10b. Generally, photocatalytic degradation efficiency of methyl orange increased when the solution pH decreased within different catalyst dosages. The results aligned to the optimum findings found in the preliminary study, in which the photocatalytic degradation of methyl orange performed more effectively under acidic conditions. This could be attributed to the surface charge of photocatalyst as well as the structural change of methyl orange under different solution pH. Besides, it was noted that solution pH affected the degradation efficiency slightly greater than the catalyst dosage. According to the results of run 1 and run 5, degradation efficiency increased from 44.49 to 57.34% when the solution pH changed from pH 7 to pH 3. Meanwhile, degradation efficiency increased from

86.72 to 94.39% when the catalyst dosage increased from 0.25 g/L in run 3 to 0.75 g/L in run 4.

Figure 10c illustrates the interaction between PMS oxidant dosage and solution pH under a constant catalyst dosage of 0.5 g/L. The findings revealed that PMS oxidant dosage had a greater effect on the photocatalytic degradation of methyl orange as compared to the solution pH. It was also noteworthy that the photocatalytic degradation efficiency could achieve higher dye degradation efficiency at lower solution pH as the PMS oxidant dosage increased from 0.2 to 0.6 mM. This was because the photocatalytic degradation process could be facilitated through the structural change of methyl orange at lower pH and also accelerated by the greater number of reactive radicals present simultaneously.

The model validation and process optimization runs were conducted simultaneously, and the results are presented in Table 5. A few optimum solutions were generated by the software according to the order of suitability. The first five solutions of the optimum conditions were selected, and experiments were conducted based on the parameter combinations. The experimental values obtained from photocatalytic degradation of methyl orange were found to be within 5% accuracy to the predicted values. For instance, the predicted degradation efficiency of 94.86% was obtained at the catalyst dosage of 0.75 g/L, oxidant dosage of 0.57 mM, and solution pH of 3.48, while the experimental value was found to be 96.63%,

**Fig. 11** Photocatalytic degradation efficiency of different types of dyes under optimized conditions

with merely 1.8% of deviation. It was noted that the experimental values obtained were in good agreement with the predicted values. Thus, it could be confirmed that the RSM method was a reliable and effective method to optimize the photocatalytic degradation of methyl orange in the studied range.

In addition, Fig. 11 presents the photocatalytic performance of g-C<sub>3</sub>N<sub>4</sub>/biochar on the degradation of different types of dyes under optimized conditions with a catalyst dosage of 0.75 g/L and PMS oxidant dosage of 0.57 mM at solution pH 3.48. The photocatalytic performance of dyes was affected by various chemical structures including azo methyl orange, diazo congo red, quinone imine methylene blue, disodium salt reactive blue, triphenylmethane malachite green, and xanthene dye rhodamine B. It was noticed that perceptible degradation of various types of dyes could be achieved, affirming that photocatalytic degradation was able to break down the dye molecule structures efficiently. The findings also proved the feasibility of g-C<sub>3</sub>N<sub>4</sub>/biochar as photocatalyst in the degradation of both azo and non-azo dyes.

## Conclusions

In this study, various biochar-based photocatalyst composites were successfully prepared using sol-gel and co-precipitation methods. SEM results depicted that biochar derived from coconut shells had plenty of meso- and macropores. The XRD and FTIR results indicated that all the characteristic peaks of metal oxides and g-C<sub>3</sub>N<sub>4</sub> could be found in their respective composite materials, which suggested that the catalysts were well incorporated on the biochar material. The composite materials exhibited good thermal stability, appropriate specific surface area, pore volume, and suitable band gap energy through the incorporation with biochar material. Among all the samples, g-C<sub>3</sub>N<sub>4</sub>/biochar was found to be the most effective photocatalyst to degrade methyl orange. The interactive effects of the operating parameters were successfully analyzed through RSM analysis. Besides, the photocatalytic degradation was optimized at the conditions with a catalyst dosage of 0.75 g/L, PMS oxidant dosage of 0.57 mM, and solution pH 3.48. Under this optimum condition, the photocatalytic degradation efficiency could achieve 96.63%. Photocatalytic degradation of methyl orange using g-C<sub>3</sub>N<sub>4</sub>/biochar was found to have followed the pseudo-first-order kinetic. In conclusion, this study was able to provide basic information on the possible utilization of biochar composites in photocatalytic degradation of organic dye. The overall results suggested that g-C<sub>3</sub>N<sub>4</sub>/biochar was a potential material to be used for the photocatalytic degradation of organic pollutants.

**Supplementary Information** The online version contains supplementary material available at <https://doi.org/10.1007/s11356-020-12251-4>.

**Acknowledgments** The authors would like to thank the anonymous reviewers for their helpful comments.

**Authors' contributions** Yean Ling Pang and Steven Lim contributed to the conception and development the design of methodology for this study. Zhi Xuan Law performed the material preparation and data collection. Zhi Xuan Law, Yin Yin Chan, and Yean Ling Pang helped to perform the analysis with constructive discussions and drafted the manuscript. Woon Chan Chong, Siew Hoong Shuit, Chin Wei Lai, and Steven Lim commented on the manuscript. All authors read and approved the final manuscript.

**Funding** This study was funded by the Fundamental Research Grant Scheme (FRGS/1/2018/TK10/UTAR/02/2) by the Ministry of Education (MOE) Malaysia, Universiti Tunku Abdul Rahman (UTAR) Research Fund (IPSR/RMC/UTARRF/2020-C2/P01) and SATU Joint Research Scheme Program.

**Data availability** All data generated or analyzed during this study are included in this published article and its supplementary materials file.

## Compliance with ethical standards

**Ethical approval** Not applicable. This manuscript does not involve researching about any animal or human data or tissue.

**Consent to participate** All of the authors consented to participate in the drafting of this manuscript.

**Consent to publish** Not applicable. All of the authors consented to publish this manuscript.

**Competing interests** The authors declare that they have no competing interests.

## References

- Ahmad I (2020) Comparative study of metal (Al, Mg, Ni, Cu and Ag) doped ZnO/g-C<sub>3</sub>N<sub>4</sub> composites: efficient photocatalysts for the degradation of organic pollutants. *Sep Purif Technol* 251:117372
- Ahmad M, Aziz ARA, Mazari SA, Baloch AG, Nizamuddin S (2020) Photocatalytic degradation of methyl orange from wastewater using a newly developed Fe-Cu-Zn-ZSM-5 catalyst. *Environ Sci Pollut Res* 27:26239–26248
- Armah EK, Chetty M, Deenadayalu N (2020) Biogas production from sugarcane bagasse with South African industrial wastewater and novel kinetic study using response surface methodology. *Scientific African* 10:e00556
- Chen D, Wang X, Zhang X, Yang Y, Xu Y, Qian G (2019) Facile fabrication of mesoporous biochar/ZnFe<sub>2</sub>O<sub>4</sub> composite with enhanced visible-light photocatalytic hydrogen evolution. *Int J Hydrog Energy* 44:19967–19977
- Costa SIG, Cauneto VD, Fiorentin-Ferrari LD, Almeida PB, Oliveira RC, Longo E, Módenes AN, Slusarski-Santana V (2020) Synthesis and characterization of Nd(OH)<sub>3</sub>-ZnO composites for application in photocatalysis and disinfection. *Chem Eng J* 392:123737
- Das A, Nikhil SK, Nair RG (2019) Influence of surface morphology on photocatalytic performance of zinc oxide: a review. *Nano-Struct Nano-Objects* 19:100353

- El Nemr A, Hassaan MA, Madkour FF (2018) Advanced oxidation process (AOP) for detoxification of Acid Red 17 dye solution and degradation mechanism. *Environmental Processes* 5:95–113
- Fazal T, Razzaq A, Javed F, Hafeez A, Rashid N, Amjad US, Ur Rehman MS, Faisal A, Rehman F (2020) Integrating adsorption and photocatalysis: a cost effective strategy for textile wastewater treatment using hybrid biochar-TiO<sub>2</sub> composite. *J Hazard Mater* 390: 121623
- Gholami P, Dinpazhoh L, Khataee A, Orooji Y (2019) Sonocatalytic activity of biochar-supported ZnO nanorods in degradation of gemifloxacin: synergy study, effect of parameters and phytotoxicity evaluation. *Ultrason Sonochem* 55:44–56
- Guo F, Lu J, Liu Q, Zhang P, Zhang A, Cai Y, Wang Q (2018) Degradation of Acid Orange 7 by peroxymonosulfate activated with the recyclable nanocomposites of g-C<sub>3</sub>N<sub>4</sub> modified magnetic carbon. *Chemosphere* 205:297–307
- Han M, Duan X, Cao G, Zhu S, Ho S-H (2020) Graphitic nitride-catalyzed advanced oxidation processes (AOPs) for landfill leachate treatment: a mini review. *Process Saf Environ Prot* 139:230–240
- Husain S, Afreen S, Hemlata, Yasin D, Afzal B, Fatma T (2019) Cyanobacteria as a bioreactor for synthesis of silver nanoparticles—an effect of different reaction conditions on the size of nanoparticles and their dye decolorization ability. *J Microbiol Methods* 162:77–82
- Karimi-Shamsabadi M, Behpour M, Babaheidari AK, Saberi Z (2017) Efficiently enhancing photocatalytic activity of NiO-ZnO doped onto nanozeoliteX by synergistic effects of p-n heterojunction, supporting and zeolite nanoparticles in photo-degradation of Eriochrome Black T and Methyl Orange. *J Photochem Photobiol A* 346:133–143
- Kruk M, Jaroniec M (2001) Gas adsorption characterization of ordered organic-inorganic nanocomposite materials. *Chem Mater* 13:3169–3183
- Li J, Xu C, Zhang Y, Tang X, Qi W, Wang Q (2018) Gravity-directed separation of both immiscible and emulsified oil/water mixtures utilizing coconut shell layer. *J Colloid Interface Sci* 511:233–242
- Li K, Huang Z, Zhu S, Luo S, Yan L, Dai Y, Guo Y, Yang Y (2019a) Removal of Cr(VI) from water by a biochar-coupled g-C<sub>3</sub>N<sub>4</sub> nano-sheets composite and performance of a recycled photocatalyst in single and combined pollution systems. *Appl Catal B* 243:386–396
- Li X, Qian X, An X, Huang J (2019b) Preparation of a novel composite comprising biochar skeleton and “chrysanthemum” g-C<sub>3</sub>N<sub>4</sub> for enhanced visible light photocatalytic degradation of formaldehyde. *Appl Surf Sci* 487:1262–1270
- Liu W, Bai X, Shen Y, Mu P, Yang Y, Li J (2020) Efficient separation of free organic liquid mixtures based on underliquid superlyophobic coconut shell coated meshes. *Sep Purif Technol* 231:115899
- Lu L, Shan R, Shi Y, Wang S, Yuan H (2019) A novel TiO<sub>2</sub>/biochar composite catalysts for photocatalytic degradation of methyl orange. *Chemosphere* 222:391–398
- Maučec D, Šuligoj A, Ristić A, Dražić G, Pintar A, Tušar NN (2018) Titania versus zinc oxide nanoparticles on mesoporous silica supports as photocatalysts for removal of dyes from wastewater at neutral pH. *Catal Today* 310:32–41
- Meng L, Yin W, Wang S, Wu X, Hou J, Yin W, Feng K, Ok YS, Wang X (2020) Photocatalytic behavior of biochar-modified carbon nitride with enriched visible-light reactivity. *Chemosphere* 239:124713
- Mian MM, Liu G, Yousaf B, Fu B, Ahmed R, Abbas Q, Munir MAM, Ruijia L (2019) One-step synthesis of N-doped metal/biochar composite using NH<sub>3</sub>-ambiance pyrolysis for efficient degradation and mineralization of Methylene Blue. *J Environ Sci* 78:29–41
- Mirzaei A, Yerushalmi L, Chen Z, Haghghat F (2018) Photocatalytic degradation of sulfamethoxazole by hierarchical magnetic ZnO@g-C<sub>3</sub>N<sub>4</sub>: RSM optimization, kinetic study, reaction pathway and toxicity evaluation. *J Hazard Mater* 359:516–526
- Mohammad A-T, Abdulhameed AS, Jawad AH (2019) Box-Behnken design to optimize the synthesis of new crosslinked chitosan-glyoxal/TiO<sub>2</sub> nanocomposite: methyl orange adsorption and mechanism studies. *Int J Biol Macromol* 129:98–109
- Nandi P, Das D (2019) Photocatalytic degradation of Rhodamine-B dye by stable ZnO nanostructures with different calcination temperature induced defects. *Appl Surf Sci* 465:546–556
- Nasir MS, Yang G, Ayub I, Wang S, Wang L, Wang X, Yan W, Peng S, Ramakrishna S (2019) Recent development in graphitic carbon nitride based photocatalysis for hydrogen generation. *Appl Catal B* 257:117855
- Norouzi O, Kheradmand A, Jiang Y, Di Maria F, Masek O (2019) Superior activity of metal oxide biochar composite in hydrogen evolution under artificial solar irradiation: a promising alternative to conventional metal-based photocatalysts. *Int J Hydrog Energy* 44:28698–28708
- Nunes LA, Silva MLS, Gerber JZ, Kalid RA (2020) Waste green coconut shells: diagnosis of the disposal and applications for use in other products. *J Clean Prod* 255:120169
- Peng X, Wang M, Hu F, Qiu F, Dai H, Cao Z (2019) Facile fabrication of hollow biochar carbon-doped TiO<sub>2</sub>/CuO composites for the photocatalytic degradation of ammonia nitrogen from aqueous solution. *J Alloys Compd* 770:1055–1063
- Peng L, Zheng R-r, Feng D-w, Yu H, Dong X-t (2020) Synthesis of eco-friendly porous g-C<sub>3</sub>N<sub>4</sub>/SiO<sub>2</sub>/SnO<sub>2</sub> composite with excellent visible-light responsive photocatalysis. *Arab J Chem* 13:4275–4285
- Pi L, Jiang R, Zhou W, Zhu H, Xiao W, Wang D, Mao X (2015) g-C<sub>3</sub>N<sub>4</sub> modified biochar as an adsorptive and photocatalytic material for decontamination of aqueous organic pollutants. *Appl Surf Sci* 358: 231–239
- Qin DD, He CH, Li Y, Trammel AC, Gu J, Chen J, Yan Y, Shan DL, Wang QH, Quan JJ, Tao CL, Lu XQ (2017) Fe<sub>2</sub>PO<sub>5</sub>-encapsulated reverse energetic ZnO/Fe<sub>2</sub>O<sub>3</sub> heterojunction nanowire for enhanced photoelectrochemical oxidation of water. *ChemSusChem* 10:2796–2804
- Shan R, Lu L, Gu J, Zhang Y, Yuan H, Chen Y, Luo B (2020) Photocatalytic degradation of methyl orange by Ag/TiO<sub>2</sub>/biochar composite catalysts in aqueous solutions. *Mater Sci Semicond Process* 114:105088
- Silvestri S, Ferreira CD, Oliveira V, Varejão JMTB, Labrincha JA, Tobaoli DM (2019a) Synthesis of PPy-ZnO composite used as photocatalyst for the degradation of diclofenac under simulated solar irradiation. *J Photochem Photobiol A* 375:261–269
- Silvestri S, Gonçalves MG, da Silva Veiga PA, da Silva Matos TT, Peralta-Zamora P, Mangrich AS (2019b) TiO<sub>2</sub> supported on *Salvinia molesta* biochar for heterogeneous photocatalytic degradation of Acid Orange 7 dye. *J Environ Chem Eng* 7:102879
- Tsamo C, Assabe M, Argue J, Ihimbru SO (2019) Discoloration of methylene blue and slaughter house wastewater using maize cob biochar produced using a constructed burning chamber: a comparative study. *Sci Afr* 3:e00078
- Wang J, Wang G, Wei X, Liu G, Li J (2018) ZnO nanoparticles implanted in TiO<sub>2</sub> macrochannels as an effective direct Z-scheme heterojunction photocatalyst for degradation of RhB. *Appl Surf Sci* 456:666–675
- Xie X, Li S, Zhang H, Wang Z, Huang H (2019) Promoting charge separation of biochar-based Zn-TiO<sub>2</sub>/pBC in the presence of ZnO for efficient sulfamethoxazole photodegradation under visible light irradiation. *Sci Total Environ* 659:529–539
- Yao Y, Cai Y, Lu F, Wei F, Wang X, Wang S (2014) Magnetic recoverable MnFe<sub>2</sub>O<sub>4</sub> and MnFe<sub>2</sub>O<sub>4</sub>-graphene hybrid as heterogeneous catalysts of peroxymonosulfate activation for efficient degradation of aqueous organic pollutants. *J Hazard Mater* 270:61–70
- Yu L, Huang Y, Yang Y, Xu Y, Wang G, Yang S (2013) Photocatalytic degradation of organic dyes by H<sub>4</sub>SiW<sub>6</sub>Mo<sub>6</sub>O<sub>40</sub>/SiO<sub>2</sub> sensitized by H<sub>2</sub>O<sub>2</sub>. *Int J Photoenergy* 2013:812376
- Yuan Y-J, Shen Z-K, Wang P, Li Z, Pei L, Zhong J, Ji Z, Yu Z-T, Zou Z (2020) Metal-free broad-spectrum PTCDA/g-C<sub>3</sub>N<sub>4</sub> Z-scheme



- photocatalysts for enhanced photocatalytic water oxidation. *Appl Catal, B* 260:118179
- Zhang H, Li M, Cao J, Tang Q, Kang P, Zhu C, Ma M (2018a) 2D a-Fe<sub>2</sub>O<sub>3</sub> doped Ti<sub>3</sub>C<sub>2</sub> MXene composite with enhanced visible light photocatalytic activity for degradation of Rhodamine B. *Ceram Int* 44:19958–19962
- Zhang L, Tu L-y, Liang Y, Chen Q, Li Z-s, Li C-h, Wang Z-h, Li W (2018b) Coconut-based activated carbon fibers for efficient adsorption of various organic dyes. *RSC Adv* 8:42280–42291
- Zhang W, Li Y, Ma X, Qian Y, Wang Z (2020) Simultaneous NO/CO<sub>2</sub> removal performance of biochar/limestone in calcium looping process. *Fuel* 262:116428
- Zhou H, Qu Y, Zeid T, Duan X (2012) Towards highly efficient photocatalysts using semiconductor nanoarchitectures. *Energy Environ Sci* 5:6732–6743
- Zhu B, Xia P, Ho W, Yu J (2015) Isoelectric point and adsorption activity of porous g-C<sub>3</sub>N<sub>4</sub>. *Appl Surf Sci* 344:188–195
- Zou H, Wang Y (2019) Functional collaboration of biofilm-cathode electrode and microbial fuel cell for biodegradation of methyl orange and simultaneous bioelectricity generation. *Environ Sci Pollut Res* 26:23061–23069

**Publisher's note** Springer Nature remains neutral with regard to jurisdictional claims in published maps and institutional affiliations.